https://doi.org/10.1007/s41230-026-5183-5

Achieving optimal strength-conductivity balance in cast Al-2.3Fe-Mg-Si alloys via Mg/Si ratio regulation

Yu-fei Zhang[1], Xi-long Luo[1], Zheng-hao Shao[1], *Qun Luo[1], Bin Hu[2], Hong-zhou Lu[3], and **Qian Li[1, 2, 4, 5]

1. State Key Laboratory of Materials for Advanced Nuclear Energy & School of Materials Science and Engineering, Shanghai University, Shanghai 200444, China

2. Chongqing Institute of New Energy Storage Materials and Equipment, Chongqing 401135, China

3. CITIC Metal Co., Ltd., Beijing 100004, China

4. College of Materials Science and Engineering, National Engineering Research Center for Magnesium Alloys, Chongqing University, Chongqing 400044, China

5. Henan Key Laboratory of Advanced Conductor Materials, Institute of Materials, Henan Academy of Sciences, Zhengzhou 450001, China

Abstract: The Al-2.3Fe eutectic alloy is regarded as a promising substitute for Cu conductors in automotive motors owing to its excellent castability and low resistivity. However, its application is restricted by the mutually exclusive relationship between electrical conductivity and mechanical strength. The microstructure and mechanical properties of Al-2.3Fe alloy were modified through Mg/Si alloying combined with T6 heat treatment in this work, leading to the development of a high-performance cast Al-2.3Fe-Mg-Si alloy. In the Al-2.3Fe-0.40Mg-0.72Si (Mg/Si=0.56) alloy subjected to T6 treatment, an electrical conductivity of (52.5±0.6)% IACS is achieved, while the ultimate tensile strength is significantly enhanced to 309.5±5.6 MPa. The addition of Mg and Si brings about marked changes in the solidification process of the Al-2.3Fe alloy, resulting in considerable variations in both the morphology of the second phase and its phase constitution. The aging behavior of the alloy is governed by second phase and solid solubility. Through optimization of the Mg/Si ratio, the aging response can be effectively enhanced. At the ratio of Mg/Si=0.56, a balance is achieved between solid solubility and precipitation, while simultaneously minimizing the detrimental impact on electrical conductivity and reaching the best mechanical properties and electrical conductivity in peak-aged Al-2.3Fe-*x*Mg-*y*Si alloy. This work providing valuable insights for developing advanced conductor materials.

Keywords: Al-Fe alloy; second phase; T6 heat treatment; electrical conductivity; mechanical properties

CLC numbers: TG146.21 **Document code:** A **Article ID:** 1672-6421(2026)03-345-12

1 Introduction

In recent years, with the advancement of the country's "dual-carbon" goal and the implementation of energy conservation and emission reduction policies, new energy vehicles, due to their low energy consumption (11.9 kWh/100 km), are gradually becoming the main alternative to fuel vehicles (45 kWh/100 km)[1, 2]. As a core component, the performance of the motor directly affects the power output and energy efficiency of the vehicle[3]. With the advancement of drive technology, rotational velocity of the motor rotor is constantly increasing, and the maximum speed can reach 20,000 rpm. This puts forward higher requirements for the strength, electrical conductivity (EC), and heat resistance of the rotor material. Aluminum alloys, with high specific strength, low cost, and excellent electrical and thermal conductivity, have become the primary choice for rotor materials[4-6]. However, existing commercial aluminum alloy systems have difficulty meeting the requirements of high conductivity and high strength simultaneously. For example, the ultimate tensile strength (UTS) of commercial A356 alloy is approximately 250 MPa, but

***Qun Luo**

Professor. Her research interest focuses on the thermodynamic and kinetic mechanism of phase transformation in magnesium and aluminum alloys.

E-mail: qunluo@shu.edu.cn

****Qian Li**

E-mail: cquliqian@cqu.edu.cn

Received: 2025-08-05; Revised: 2025-11-11; Accepted: 2025-12-16

its EC is less than 40% IACS[7-10]. The EC of commercial 1070 alloy reaches up to 60% IACS, yet its strength is lower than 30 MPa[11]. The rotor material of the drive motor for new energy vehicles needs to maintain an EC of not less than 50% IACS and a yield strength of not less than 60 MPa at a service working temperature of 180 °C[12]. Therefore, the development of new Al alloys with both high EC and high strength has become an urgent problem to be solved.

In conventional strengthening approaches, the primary factors include solute elements, second phases, grain boundaries, and dislocations. Nevertheless, these elements hinder and scatter the movement of free electrons, resulting in a mismatch between the mechanical properties and EC of the alloy[13-15]. Owing to its precipitation characteristics, the Al-Mg-Si alloy demonstrates superior mechanical properties and EC following artificial aging treatment[15-17]. Modulating the Mg/Si ratio can increase the size and quantity of precipitates in matrix, thus achieving the synergistic improvement of strength and EC[18]. However, with the progress of aging, these precipitates undergo transformation and coarsening, leading to a reduction in the strength of the Al alloy[19]. In a relatively high-temperature environment, cast Al-Mg-Si alloys exhibit performance degradation, and this instability limits their applications.

Lattice distortion resulting from elemental solid solution is a key factor affecting the EC of alloys. The low solubility of Fe in the Al matrix (approximately 0.052wt.%) results in its resistivity contribution being far lower than that of the second phase[20, 21]. Therefore, Al-Fe alloys have been applied to motor rotors and electrical transmission devices[22-26]. However, as a new type of cast Al alloy, the coarse Fe-rich phase in as-cast Al-Fe alloys reduced the formability and workability. Microalloying elements significantly influence the properties of Al-Fe alloys through distinct mechanisms. Ce addition refines grains and optimizes Al_3Fe phase morphology while promoting discontinuous Fe-rich networks[27], Co-addition of Er and Zr transforms needle-like Al_3Fe into rod-shaped particles, simultaneously enhancing strength and conductivity[28]. Shi et al.[29] proposed that Ce can also facilitate the formation of a discontinuous network or granular structure of the Fe-rich phase, thereby enhancing the uniformity and mechanical properties of the alloy. Shin et al.[30] found that the solidification path in the Al-1Fe-*x*(Mg/Si) alloy are not affected by the initial Si/Fe ratio, but depend on the segregation of Si and Mg content. The addition of Ni has been shown to significantly enhance the mechanical properties, electrical conductivity, and thermal stability of Al-Fe alloys by refining the grain size and promoting the formation of the thermally stable Al_9FeNi phase[31-34]. Trink et al.[35] proposed that by adding Mg and Si to the Al-Fe alloy, it can be given age-hardening ability, thereby improving its comprehensive properties. Tao et al.[36] demonstrated that regulating the Mg/Si ratio in Al-Mg-Si-Cu alloys effectively suppresses the negative natural aging effect, as the formation of stable Si-rich clusters promotes the synchronous nucleation of fine β" precipitates during subsequent artificial aging. Therefore, Mg and Si alloying and controlling the Mg/Si ratio represent potential approaches to simultaneously enhance the mechanical properties and electrical conductivity of cast Al-Fe alloys.

The relationships among alloy composition, microstructure, mechanical properties, and EC remain unclear on cast Al-Fe alloys. This work focused on the Al-2.3Fe alloy, the influence mechanism of different Mg and Si contents and Mg/Si ratios on the types and morphologies of the second phase and their effects on the EC and mechanical properties, and also studied the evolution of the microstructure and properties of the Al-2.3Fe-*x*Mg-*y*Si alloy during heat treatment. By means of micro-alloying and aging treatment, the shape and dispersion of the second phase, element distribution, and nano-precipitates are controlled, and a casting Al-2.31Fe-0.40Mg-0.72Si alloy with both high strength and high EC is obtained.

2 Experiments

The thermodynamic calculations conducted in this study utilized the Pandat software package and PanAl thermodynamic database (both developed by CompuTherm LLC), yielding the solidification paths and elemental solubilities of the Al-2.3Fe-*x*Mg-*y*Si alloys.

The Al-2.3Fe-*x*Mg-*y*Si alloys in this study were prepared using commercial pure Al, Al-20Fe master alloy, Al-50Mg master alloy, and Al-20Si master alloy. The pure Al was sourced from Shandong Xiangruida Aluminum Industry Co., Ltd., while the Al-20Fe master alloy, Al-20Si master alloy, and Al-50Mg master alloy were provided by Shanghai Qichen Industrial Co., Ltd. In the course of melting, these raw materials were placed into a clean graphite crucible and heated in a resistance furnace. The Al particles were initially melted at a temperature of 800 °C. Subsequently, pre-dried Al-20Si master alloy and Al-20Fe master alloy were added, followed by a 1 h holding period to guarantee full melting. After that, the molten alloy was maintained at a reduced temperature of 740 °C for 0.5 h, after which Al-50Mg master alloy was added to the melt and held for another 0.5 h. During the holding period, the melt was stirred for 30 s every 20 min to ensure uniform composition of the melt. The resulting homogeneous melt was purified using 0.5wt.% Foseco flux. High-purity argon gas was purged for 3 min to further degas and remove impurities. Afterward, the molten alloy was poured into a *Φ*30 mm cylindrical steel mold and a permanent mold for *Φ*10 mm tensile bars, respectively. These molds were preheated to 250 °C. The as-cast specimens were subjected to T6 heat treatment: solution treatment at 520 °C for 4 h, followed by water quenching to room temperature, and then artificial aging at 180 °C for 0 h, 20 h, and 150 h respectively, so as to obtain solution treated samples, peak-aged samples, as well as the age-hardening curves over the 150 h aging process.

The actual chemical composition of the alloys was measured using Inductively Coupled Plasma Atomic Emission

Spectroscopy (ICP-AES), with the test findings presented in Table 1.

Table 1: Nominal and actual compositions of Al-2.3Fe-*x*Mg-*y*Si alloys

Samples	Actual composition (wt.%)	Mg/Si ratio
0Mg-0Si	Al-2.32Fe	/
0.7Mg-0Si	Al-2.06Fe-0.74Mg	/
0.3Mg-0.7Si	Al-2.23Fe-0.31Mg-0.73Si	0.42
0.4Mg-0.7Si	Al-2.31Fe-0.40Mg-0.72Si	0.56
0.5Mg-0.9Si	Al-2.39Fe-0.53Mg-0.85Si	0.62
0.7Mg-0.7Si	Al-2.33Fe-0.65Mg-0.70Si	0.93

The phase morphology and phase constitution of the as-cast alloy and heat-treated alloy were analyzed by XRD using a Bruker D8 diffractometer. Scanning was performed at a rate of 2°·min^{-1} in the range of 20°–50°, and a more detailed scan was conducted in the range of 15°–35° with a step size of 0.02° and a dwell time of 1 s. After polishing, the alloy samples were etched by immersion in a 5% NaOH aqueous solution for 20 s. The microstructure and phases of the alloy were analyzed by SEM-EDS using a Hitachi FLEX-1000.

The hardness of the alloy was tested using a Vickers hardness tester, with a load of 200 gf and a dwell time of 10 s, five measurement results were obtained and the average hardness was taken. Room-temperature tensile tests were carried out with an MTS Landmark379 testing system, at a tensile speed of 1 mm·min^{-1} and a strain rate of 3.7×10^{-4} s^{-1}. For each alloy, three groups of stress-strain tests were conducted to calculate the average yield strength (YS), ultimate tensile strength (UTS), and elongation (EL). The EC was measured using a PZ 60A eddy current conductivity meter, with a test frequency of 60 kHz. Before testing, the samples were polished with #1200 and #2000 metallographic sandpapers to ensure a smooth surface. For each alloy, 15 random measurements were conducted to obtain the average value of EC.

3 Results and discussion

3.1 Performance improvement and microstructure evolution of as-cast alloys

Six groups of samples listed in Table 1 were prepared to examine how microalloying with Mg and Si affects the properties and microstructure of the alloy in this work. Stress-strain tests were performed on the six as-cast alloys, and the results are shown in Figs. 1(a) and (b). Although the YS and UTS of the 0Mg-0Si alloy without Mg and Si addition are only 45.0±2.1 MPa and 110.2±0.1 MPa, the EL reaches (34.0±3.7)%. After only adding 0.7wt.% Mg, both the YS and UTS of the Al-2.3Fe alloy increases significantly, to 52.0±3.1 MPa and 142.3±4.2 MPa respectively, but the EL slightly decreases to (25.7±0.6)%. The decrease in EL may be caused by the addition of Mg changing the original phase constitution in Al-2.3Fe. Noting that among the as-cast alloys with combined addition of Mg and Si, the 0.4Mg-0.7Si alloy with a Mg/Si ratio of 0.56 shows the optimal overall mechanical properties. Its YS and the UTS are 63.4±3.7 MPa and 184.8±2.4 MPa respectively, which are increased by 40.9% and 67.7% compared with the 0Mg-0Si alloy, and the EL slightly decreases to (25.4±1.0)%. When Mg and Si were added together, the strength of the alloy further increased. Notably when the combined addition amount of Mg and Si exceeded ~1wt.%, the UTS of the as-cast Al-2.3Fe alloy stayed at a similar level.

The YS-EC distribution diagram of cast Al alloy is shown in Fig. 1(c). Compared with Al-0.5Fe-X alloy[37], Al-Mg alloy[32], and pure Al, the addition of Mg and Si brings a YS advantage in as-cast Al-2.3Fe alloys. The mechanical properties of Al-2.3Fe-*x*Mg-*y*Si alloys reach the level of refined Al-Fe-Ni alloy. However, the decrease in EC makes the alloy lose its performance advantage. After T6 heat treatment, both the EC and YS of the alloy have significantly increased. This phenomenon will be analyzed in the subsequent.

The strength-plasticity product of an alloy is a key indicator for evaluating its comprehensive mechanical properties, as it can reflect the material's ability to balance strength and plasticity. In this study, the strength-plasticity products of the six alloys were calculated to screen the alloy composition with the optimal comprehensive performance and effectively reflect the impacts of Mg and Si on the strength and plasticity of the Al-2.3Fe alloy. The result of the strength-ductility product and EC is shown in Fig. 1(d). Due to the lowest content of solid solution elements in the matrix, the 0Mg-0Si alloy exhibits the best EC performance, reaching (55±0.3)% IACS. As Mg and Si are added simultaneously, the EC of the alloy decreases sharply and remains at the same EC level around 44% IACS with the increase of Mg and Si. The strength-ductility products of alloys 0.4Mg-0.7Si, 0.5Mg-0.9Si, and 0.7Mg-0.7Si in the as-cast state all exceed 4 GPa%, reaching 4.7 GPa%, 4.4 GPa% and 4.1 GPa%, respectively.

To investigate the strengthening mechanisms of Mg and Si in as-cast Al-2.3Fe alloys, the microstructures of six samples were characterized by SEM-BSE, with the findings presented in Fig. 2. Figures 2(a) and (a1) show the morphology of the second phase of the Al-2.3Fe alloy. Given that Fe has low solid solubility in the Al matrix, the Al-2.3Fe alloy without Mg and Si additions forms numerous fibrous rod-like Al-Fe binary intermetallics distributed in a dense network. Meanwhile, solute segregation leads to the formation of a small quantity of granular secondary phases at the grain boundaries. Based on the results of SEM-EDS, the phase in the alloy is determined to be the $Al_{13}Fe_4$ phase. This eutectic structure with a network distribution does not disrupt the continuity of the matrix and can produce more uniform plastic deformation under stress. Therefore, the 0Mg-0Si alloy has the highest EL, reaching (34.0±3.7)%. The introduction of Mg alteres the morphology of the second phase, as illustrated in Figs. 2(b) and (b1). Different from 0Mg-0Si alloy, the second phase changed from dense fibrous rod-like to coarse lath shapes. Although the

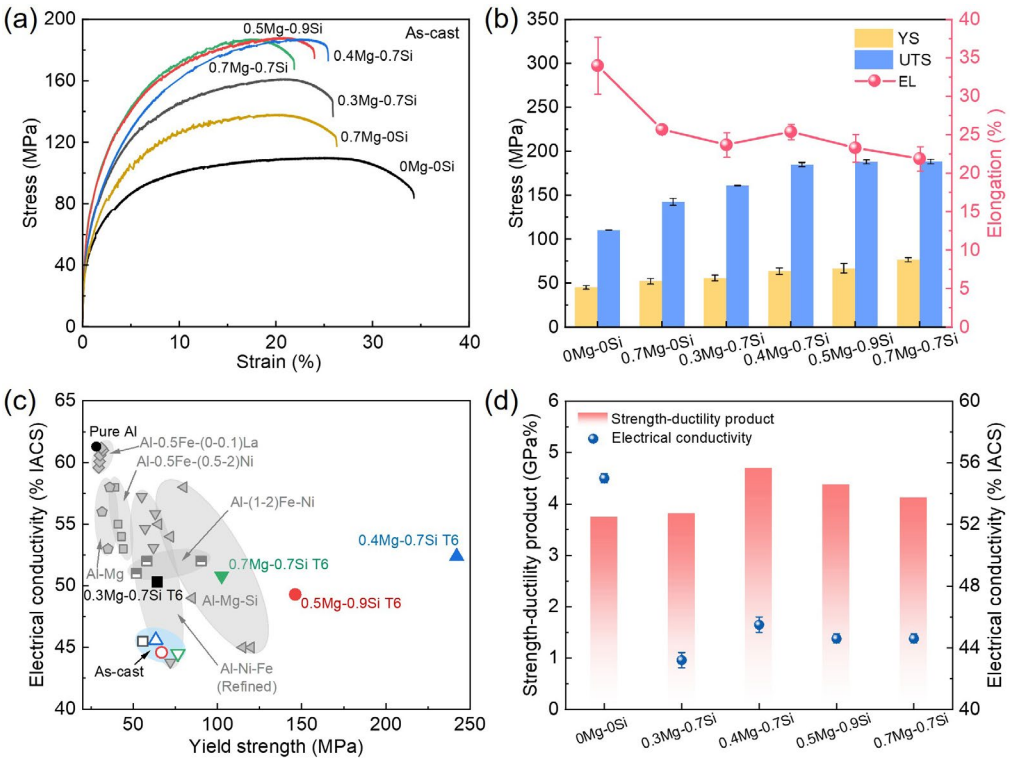

Fig. 1: Stress-strain curves of as-cast Al-2.3Fe-*x*Mg-*y*Si alloys (a), mechanical properties of the Al-2.3Fe-*x*Mg-*y*Si alloy (b), distribution of YS-EC for casting Al alloys (c), and distribution of the strength-ductility products and EC in as-cast Al-2.3Fe-*x*Mg-*y*Si alloy (d)

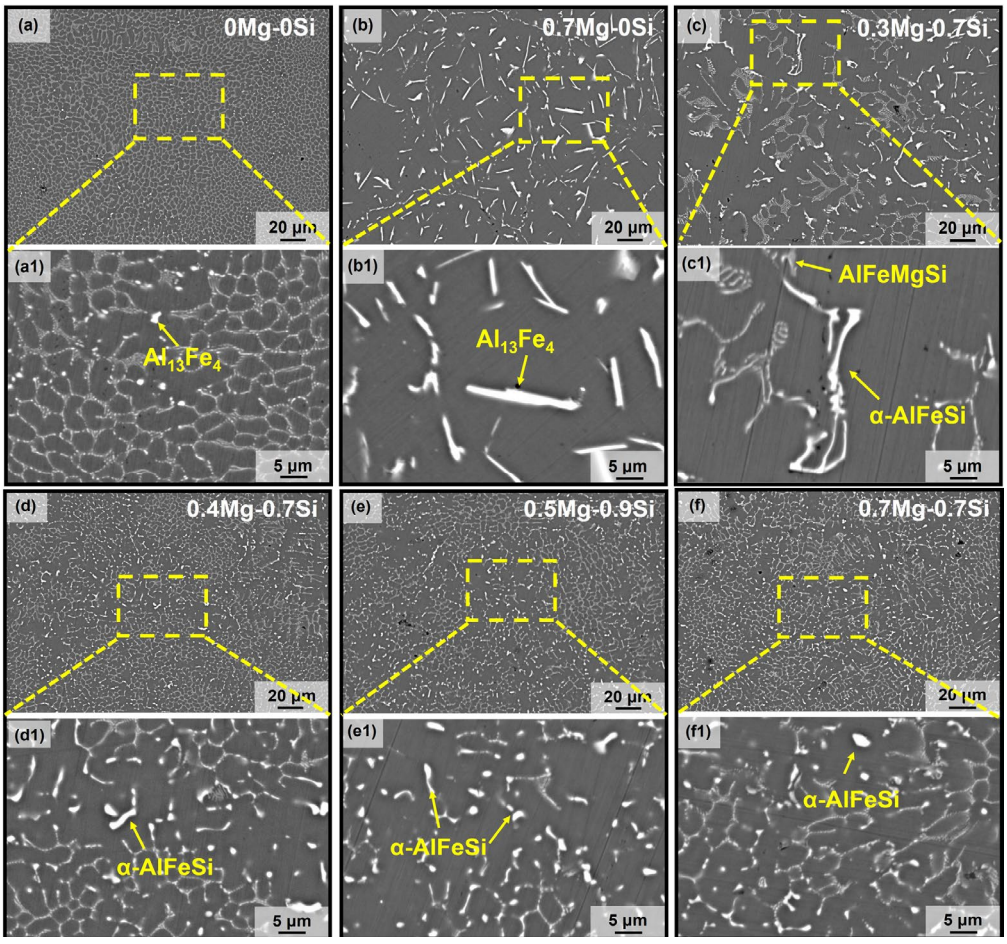

Fig. 2: SEM images of as-cast Al-2.3Fe-*x*Mg-*y*Si alloys: (a, a1) 0Mg-0Si; (b, b1) 0.7Mg-0Si; (c, c1) 0.3Mg-0.7Si; (d, d1) 0.4Mg-0.7Si; (e, e1) 0.5Mg-0.9Si; (f, f1) 0.7Mg-0.7Si

phase is still the $Al_{13}Fe_4$, strong stress concentration occurres at both ends of the lath-shaped second phase. It is prone to becoming a crack source during the deformation. Therefore, the EL of 0.7Mg-0Si alloy decreases significantly. At the same time, the solid solution of Mg heightens lattice distortion within the Al matrix, contributing to a rise in strength. When Mg and Si are added together in the Al-2.3Fe alloy, new phases are generated. As can be seen from Figs. 2(c) and (c1), in addition to the reticular eutectic structure in 0.3Mg-0.7Si alloy, blocky AlFeMgSi phase and skeletal AlFeSi phase are formed. The introduced new phases disrupt the continuity of the eutectic structure. When the total content of Mg and Si in the Al-2.3Fe alloy exceeds 1wt.%, a dense reticular structure is formed in the alloy, as shown in Figs. 2(d–f) and Figs. 2(d1–f1). The 0.4Mg-0.7Si, 0.5Mg-0.9Si, and 0.7Mg-0.7Si alloys have similar microstructures. In addition to the eutectic structure, the blocky phase is also formed. This phase is identified as the α-AlFeSi phase through SEM-EDS (Fig. 3). Due to the similar phase and microstructure, the 0.4Mg-0.7Si, 0.5Mg-0.9Si, and 0.7Mg-0.7Si alloys have similar mechanical properties, but there are slight differences in EC. This may be caused by the different Mg/Si ratios resulting in different contents of the blocky phase.

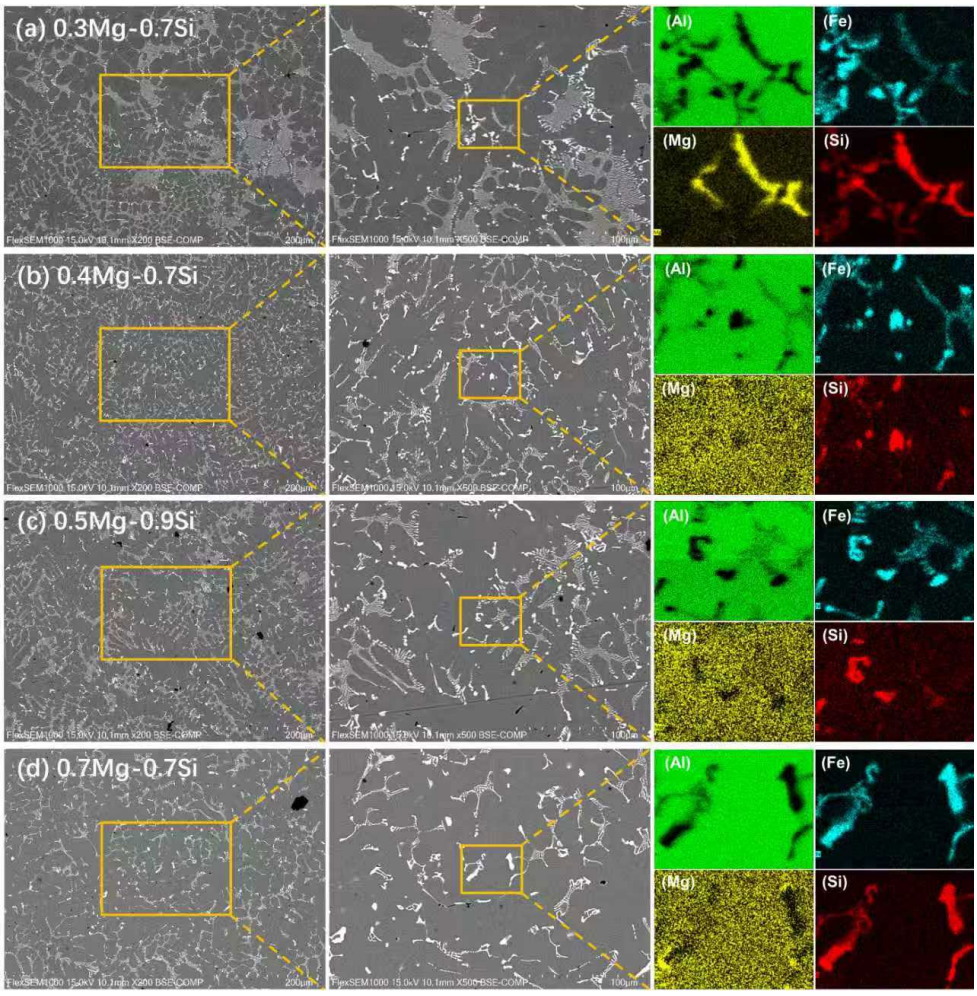

Fig. 3: Second phases and elemental distribution in Al-2.3Fe-*x*Mg-*y*Si alloys

The grain size of the alloy was characterized by anodization and polarized light grain size measurement, and the results are shown in Fig. 4. The average grain size of the alloys was statistically examined via the intercept method. The grain sizes of 0.3Mg-0.7Si, 0.4Mg-0.7Si, 0.5Mg-0.9Si, and 0.7Mg-0.7Si alloys are 245±36 μm, 221±18 μm, 232±21 μm, and 221±25 μm, respectively. The grain sizes of all samples are comparable, which confirms the consistency of alloy preparation and the rationality of microstructural analysis.

Further analyze the phases in the alloy through XRD. To facilitate the analysis of the second-phase constitution, the spectral peaks were magnified, and the results are shown in Fig. 5. The characteristic peak positions and peak intensities of the phases in these alloys are different, indicating that the phases and their contents in the Al-2.3Fe alloy have changed with the introduction of Mg and Si as well as the change of their contents. When only Mg is added to the Al-2.3Fe alloy, only the characteristic peak of the $Al_{13}Fe_4$ phase appears in the alloy. Mg is primarily dissolved in the Al matrix, exerting a solid solution strengthening effect. After the simultaneous addition of Mg and Si, the phase constitution of the alloy changes significantly, with the characteristic peaks of the β-AlFeSi phase and α-AlFeSi phase appearing. In the 0.3Mg-0.7Si alloy, distinct diffraction peaks of the β-AlFeSi phase are observed.

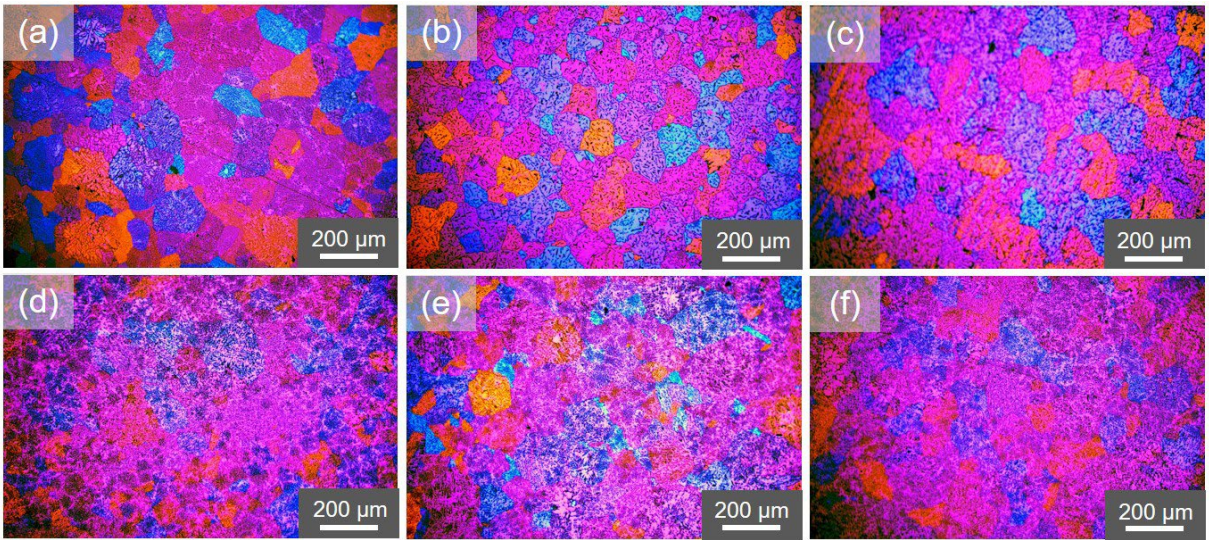

Fig. 4: Polarized grain images of as-cast Al-2.3Fe-*x*Mg-*y*Si alloys: (a) 0Mg-0Si; (b) 0.7Mg-0Si; (c) 0.3Mg-0.7Si; (d) 0.4Mg-0.7Si; (e) 0.5Mg-0.9Si; (f) 0.7Mg-0.7Si

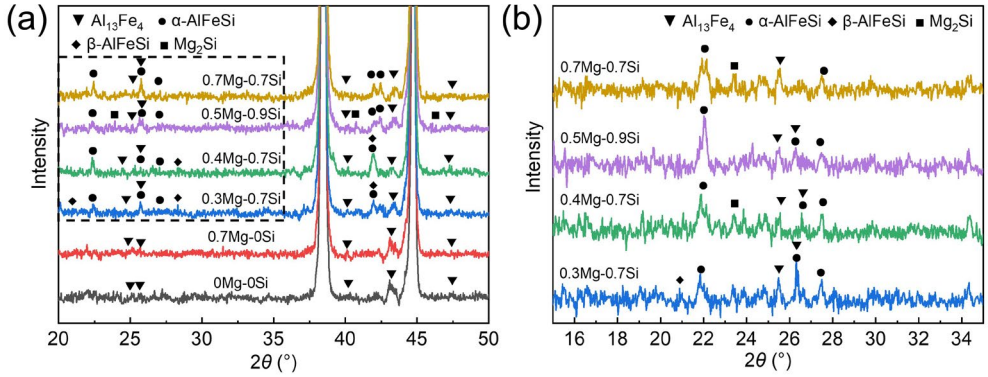

Fig. 5: XRD patterns of as-cast Al-2.3Fe-*x*Mg-*y*Si alloys: (a) 20°–50°; (b) 15°–35° fine scanning

When the Mg/Si ratio exceeds 0.5, in the 0.4Mg-0.7Si alloy, the diffraction peaks of the β-AlFeSi phase diminish and their intensity decreases, in the 0.5Mg-0.9Si and 0.7Mg-0.7Si alloys, the characteristic peaks of the β-AlFeSi phase has disappeared, while those of the α-AlFeSi phase gradually intensify. Meanwhile, in the fine scanning results [Fig. 5(b)] within the range of 15°–35°, diffraction peaks of the Mg_2Si phase are observed in the 0.4Mg-0.7Si and 0.7Mg-0.7Si alloys, and the content of Mg_2Si in the alloy is relatively high. This indicates that the types and content of phases in the alloy are influenced by the Mg/Si ratio.

Adding Mg and Si together modifies the properties of the as-cast Al-2.3Fe alloy in three aspects. Firstly, the solution of Mg and Si enhances the mechanical properties of the alloy. However, the atoms dissolved in the matrix increase electron scattering, resulting in a significant decrease in EC. Secondly, due to the combined addition of Mg and Si, the composition and content of the second phase in the alloy change, and the increase in the second phase content is the main reason for the improvement of the alloy's mechanical properties. Thirdly, the Mg/Si ratio affects the microstructure of the alloy. As the Mg/Si ratio increases, the microstructure is refined. But more massive α-AlFeSi phases are formed and leading to a decrease in the EC.

3.2 Evolution of microstructure and properties during heat treatment

Heat treatment stands as a key approach to regulating the properties of cast alloys[38-40]. Meanwhile, the nano-precipitation can reduce the solid solubility of elements in the Al matrix to a certain extent and decrease the electron scattering in the Al matrix[13].

The evolution of hardness and EC of the six alloys during the T6 heat treatment is shown in Fig. 6. The hardness of the

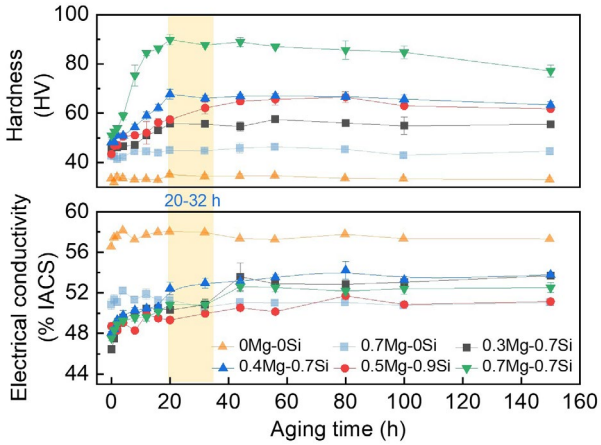

Fig. 6: Age-hardening curves of Al-2.3Fe-*x*Mg-*y*Si alloys

0Mg-0Si alloy without the addition of Mg and Si does not change with aging, indicating that the Al-2.3Fe alloy does not have the aging strengthening. The solid solution of Mg is increased in 0.7Mg-0Si alloy, but there is no improvement in performance during aging. Obviously, the introduction of Mg did not result in the formation of precipitation. It is worth noting that the EC of both 0Mg-0Si alloy and 0.7Mg-0Si alloy increased in the initial 1–4 h of the aging process. This can be attributed to the decrease in lattice defects like dislocations and vacancies, which lessened electron scattering and in turn boosted the EC.

As a structural component in the precipitates of the Al-Mg-Si system, Si plays a crucial role in the nucleation and growth of precipitates[41-43]. When Mg and Si are added in combination, the alloy exhibits obvious age-hardening effects within 0–20 h. The hardness of 0.3Mg-0.7Si alloy increases from 45.6 HV in the solution to 55.8 HV at peak aging (20–32 h). The hardness of 0.4Mg-0.7Si alloy increases from 48.2 HV in the solution to 67.8 HV in the peak-aged (20–32 h). The hardness of 0.5Mg-0.9Si alloy increases from 43.4 HV in the solution to 62.0 HV in the peak-aged (20–32 h). The hardness of 0.7Mg-0.7Si alloy increases from 51.0 HV in the solution to 89.9 HV in the peak-aged (20–32 h). As the aging time increases, the hardness of all alloys decreases to some extent and then tends to be stable, the EC of the four alloys exhibits a trend of gradual increase followed by stabilization, reaching 53.9% IACS, 53.8% IACS, 50.9% IACS, and 52.5% IACS, respectively. Unlike the trend of hardness change, the stabilization of EC shows a certain hysteresis during aging. This is due to the transformation of the β" phase into the β phase upon entering the over-aging stage, accompanied by the conversion of the semi-coherent interface between β" and α-Al into a coherent interface between β and α-Al[4]. As a result, the lattice distortion decreases and electron scattering is reduced.

In terms of hardness and EC performance, there is no positive correlation between the age-hardening effect and the total content of added Mg and Si. Instead, adjusting the Mg/Si ratio can enhance the age-hardening effect. Specifically, the age-hardening effects of the 0.4Mg-0.7Si and 0.7Mg-0.7Si alloys are superior to those of the 0.5Mg-0.9Si alloy. In other words, the Al-2.3Fe-*x*Mg-*y*Si alloys achieve the optimal age-hardening effect when the Mg/Si ratio is 0.56 or 0.93. Notably, the hardness of the 0.4Mg-0.7Si alloy decreases by only 4 HV compared with that at peak aging, and its electrical conductivity increases to 53% IACS and stabilizes after 150 h for aging. This change in the EC and hardness indicate that the designed alloy has excellent high-temperature stability.

The mechanical properties of the solution 0.3Mg-0.7Si, 0.4Mg-0.7Si, 0.5Mg-0.9Si and 0.7Mg-0.7Si alloys are shown in Figs. 7(a–b). Compared with the as-cast state, the UTS of these solution alloys has decreased by approximately 40 MPa. The YS of 0.3Mg-0.7Si, 0.4Mg-0.7Si, 0.5Mg-0.9Si and 0.7Mg-0.7Si alloys reached 51.4±5.4MPa, 65.8±3.7 MPa, 61.9±8.2 MPa, 63.2±2.4 MPa, respectively. The EL of 0.3Mg-0.7Si, 0.4Mg-0.7Si, 0.5Mg-0.9Si and 0.7Mg-0.7Si alloys reached (30.7±1.9)%, (29.4±6.9)%, (26.4±2.5)% and (27.8±1.5)%, respectively. The mechanical properties of 0.4Mg-0.7Si to 0.7Mg-0.7Si alloys remain at the same level.

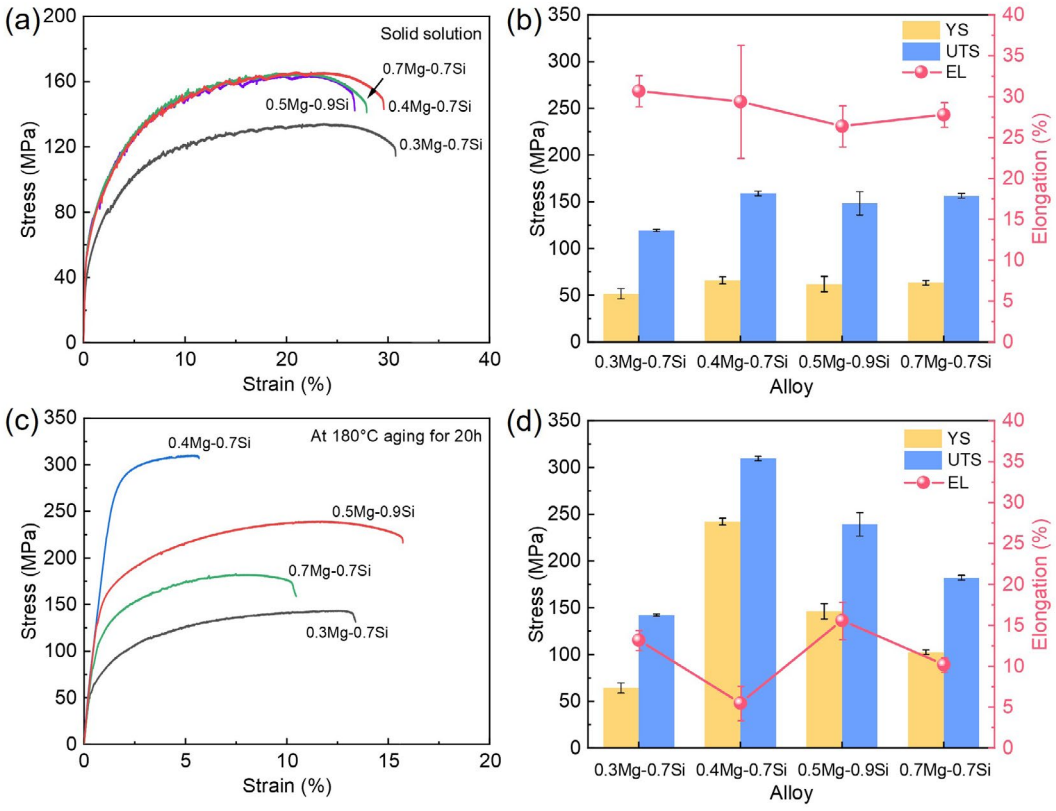

Fig. 7: Stress-strain curves and mechanical properties of Al-2.3Fe-*x*Mg-*y*Si alloys under different heat treatment states: (a–b) solution; (c–d) peak-aged

The difference is that due to the solution treatment causing partial dissolution of the second phase, the EL of the solution alloy is increased compared with the as-cast state.

Different Mg/Si ratios exert a notable influence on the age-hardening effect of the alloy. The mechanical properties of the aged alloys are shown in Figs. 7(c–d). Different from the hardness, after 20 h of aging treatment, 0.4Mg-0.7Si alloy exhibits the best strength. The UTS and YS reach 309.5±5.6 MPa and 242.1±7.2 MPa, respectively, but the EL decreases to (5.5±2.1)% after T6 heat treatment. 0.3Mg-0.7Si, 0.5Mg-0.9Si, and 0.7Mg-0.7Si alloys all exhibit different aging strengthening effects. Under the same aging time, compared with the solution state, the UTS increases by 22.9 MPa, 91.0 MPa, and 25.7 MPa, respectively, and the EL decreases by 17.5%, 10.8%, and 17.6%, respectively. When the Mg/Si ratio is 0.56, the 0.4Mg-0.7Si alloy has the best aging strengthening in mechanical properties.

To further elaborate on how heat treatment affects the alloy's properties, the microstructure of the alloy during the heat treatment was characterized by SEM, and BSE images of the solution and aged microstructures were obtained. The results are presented in Figs. 8 and 9. In comparison with the as-cast alloy, following solution treatment at 520 °C, the fibrous rod-like eutectic structure and massive second phase undergo spheroidization and coarsening, while the morphology of the lath-like second phase does not change significantly. Compared with the solution-treated microstructure, the second phase of the alloy after 20 h of aging undergoes further coarsening, and the continuity of the eutectic structure is disrupted. It is worth noting that the morphology of the second phase in 0.4Mg-0.7Si alloy completely transforms into dispersed spherical particles after aging treatment.

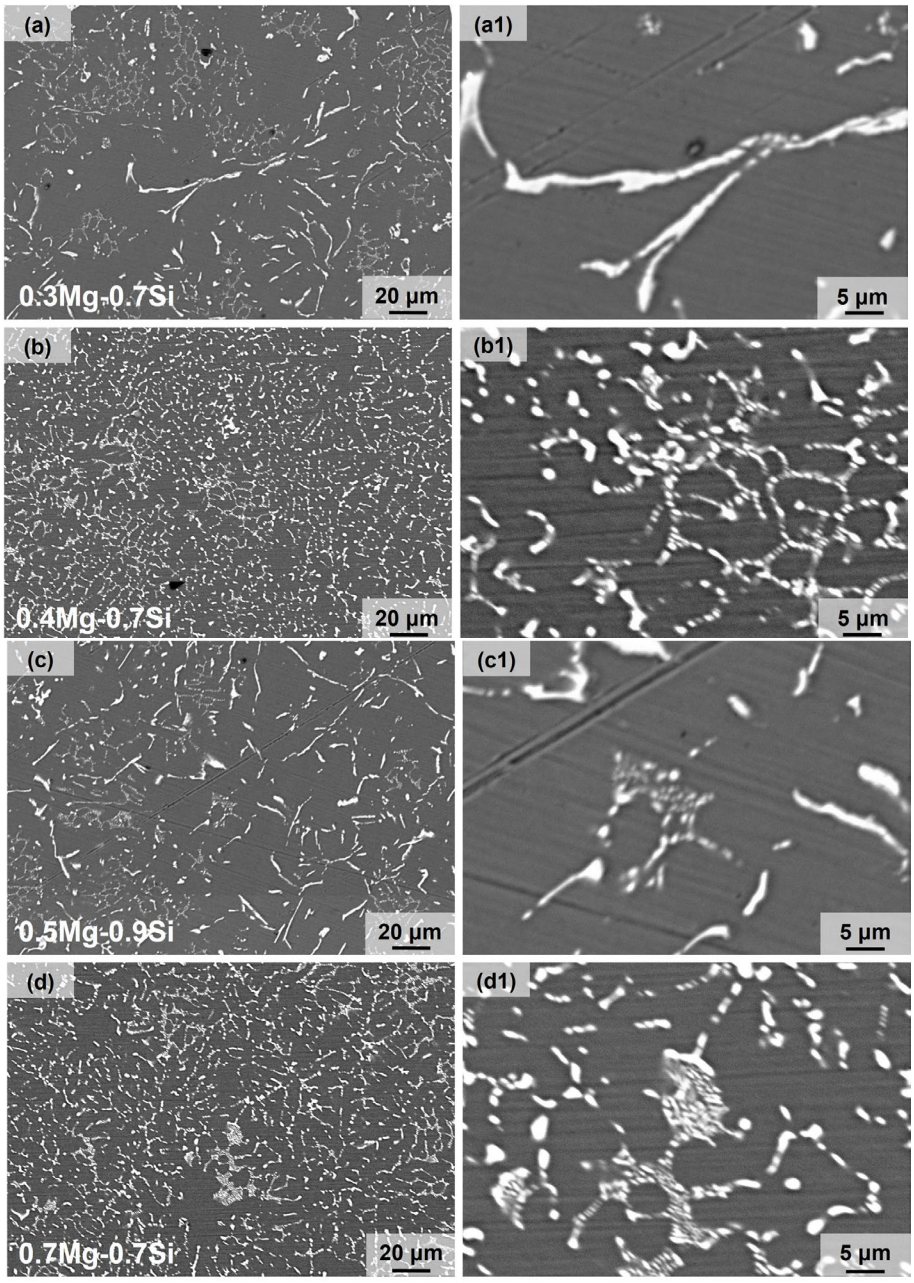

Fig. 8: SEM images of solution Al-2.3Fe-*x*Mg-*y*Si alloys: (a, a1) 0.3Mg-0.7Si; (b, b1) 0.4Mg-0.7Si; (c, c1) 0.5Mg-0.9Si; (d, d1) 0.7Mg-0.7Si

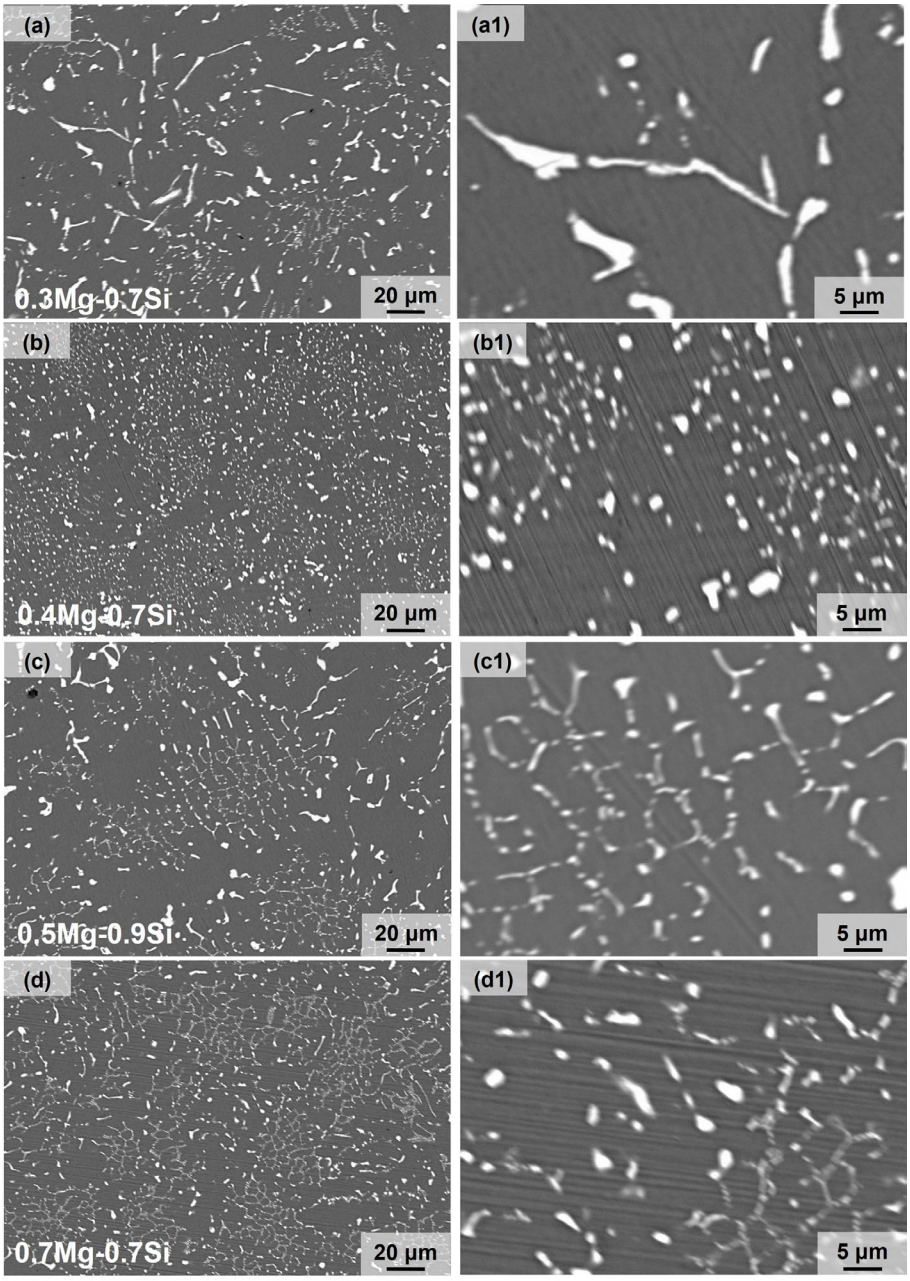

Fig. 9: SEM images of peak-aged Al-2.3Fe-*x*Mg-*y*Si alloys: (a, a1) 0.3Mg-0.7Si; (b, b1) 0.4Mg-0.7Si; (c, c1) 0.5Mg-0.9Si; (d, d1)0.7Mg-0.7Si

3.3 Effect of Mg/Si ratio on age-strengthening of Al-2.3Fe-*x*Mg-*y*Si alloys

To examine the effect of the Mg/Si ratio on the alloy's microstructure, image segmentation was carried out on the microstructures of the alloy under different states, with classification based on the size of the second phase. The aspect ratio and area fraction of the second phase were extracted and statistically analyzed, and the result are shown in Fig. 10. With the addition of Mg and Si, the area fraction of second phase in as-cast alloys first declines significantly and subsequently rise in a gradual manner. From the distribution of the aspect ratio of the phases, when the Mg/Si ratio is greater than 0.5, the microstructure in the Al-2.3Fe-*x*Mg-*y*Si alloys is significantly refined, and the phase area fraction increases from 7.9% of 0.3Mg-0.7Si alloy to more than 10%. Among them, the second phase area fraction of 0.4Mg-0.7Si alloy reaches 11.3%. Although heat treatment does not significantly change the phase area fraction, but solution treatment causes a reduction in the aspect ratio of the second phase, leading to its spheroidization and coarsening, as shown in Figs. 10(a) and (b). The second phase undergoes further spheroidization and coarsening after aging, as shown in Fig. 10(c). Attributed to the difference in plasticity between the coarsened brittle second phase and the Al matrix, the second phase is prone to generating microcracks during the deformation and further expanding to cause fracture, resulting in the deterioration of the EL after heat treatment.

Phase diagram calculations were conducted to identify the solidification paths of the six alloys under non-equilibrium solidification conditions, with the outcomes shown in Fig. 11(a).

The introduction of Mg retards the diffusion process in the melt, which increases the solidification range of the Al-2.3Fe alloy from 1 °C to 206 °C and facilitates the formation of coarse plate-like $Al_{13}Fe_4$ phases.

The combined addition of Mg and Si alters the reaction sequence, leading to the formation of AlFeMgSi phases and α-AlFeSi phases after α-Al. The rapid consumption of alloying elements in the melt reduces the solidification range to 100 °C, resulting in microstructural refinement. The four alloys with distinct Mg/Si ratios exhibit similar solidification processes, but variations in elemental composition lead to differences in phase fractions.

In terms of the hardness and mechanical property results, the age-hardening effect of the Al-2.3Fe-*x*Mg-*y*Si alloys is influenced by both the total content of Mg and Si and the Mg/Si ratio. Specifically, when the Mg/Si ratio is 0.56, T6 heat treatment can notably enhance the alloy's mechanical properties. When the Mg/Si ratio is 0.93, the contribution of heat treatment to hardness is significantly greater than that to strength, and the alloy achieves the optimal age-hardening effect in terms of hardness.

To analyze the differences in age-hardening effects among alloys with different Mg/Si ratios, the solid solubility of Mg and Si in α-Al was computed, and the corresponding results are presented in Fig. 11(b). The solid solubility of these elements in α-Al determines the aging potential of the alloys. The solid solubility curve of Mg follows a consistent trend, exhibiting a positive correlation with Mg content. In contrast, the formation of α-AlFeSi phases consumes a significant amount of Si atoms, resulting in a rapid decline in the solid solubility of Si in α-Al during the initial stages of solidification. Among the alloys, the 0.7Mg-0.7Si alloy exhibits the highest Mg solid solubility

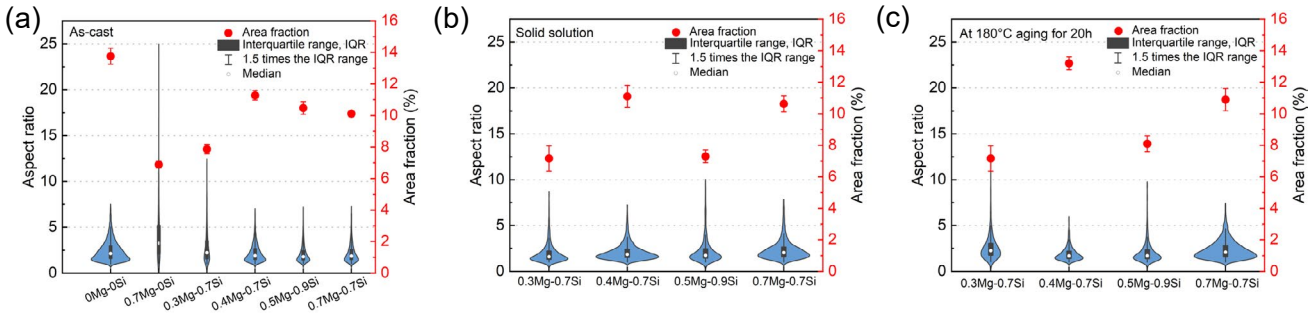

Fig. 10: Microstructure characteristics of Al-2.3Fe-*x*Mg-*y*Si alloys: (a) as-cast; (b) solid solution; (c) peak-aged

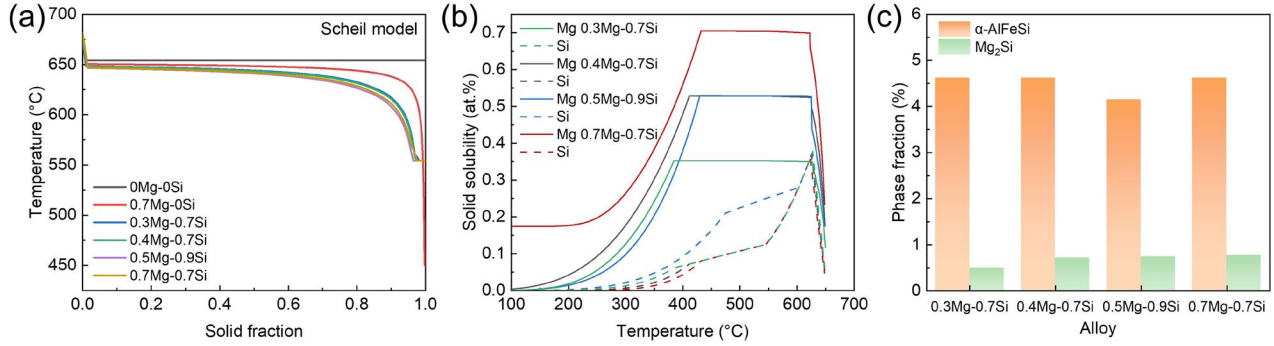

Fig. 11: Solidification paths of Al-2.3Fe-*x*Mg-*y*Si alloys based on Scheil model (a), solid solubility of Mg and Si in α-Al of Al-2.3Fe-*x*Mg-*y*Si alloys (b), and phase fraction calculated at 180 °C (c)

but the lowest Si solid solubility, resulting in divergent trends in hardness and strength properties. The phase fractions of the alloys at 180 °C are presented in Fig. 11(c). The calculations reveal that the 0.4Mg-0.7Si and 0.7Mg-0.7Si alloys possess the highest fractions of α-AlFeSi and Mg_2Si phases, resulting in the most pronounced age-hardening effect.

The distribution of electrical conductivity and hardness in the Al-2.3Fe-*x*Mg-*y*Si alloys during a 150 h aging process is shown in Fig. 12. Different Mg/Si ratios bring different degrees of improvement to the conductivity and hardness. For alloys with low Mg contents and low Mg/Si ratios, such as 0.3Mg-0.7Si, aging treatment can significantly enhance EC, but the increase in alloy hardness is not pronounced. When the

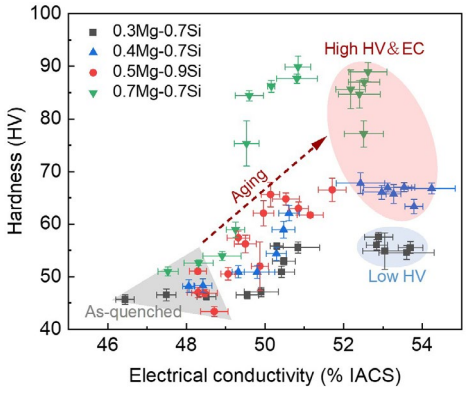

Fig. 12: Distribution of EC and hardness in Al-2.3Fe-*x*Mg-*y*Si alloys after aging for 150 h

Si content is high, the aging treatment can increase both the EC and hardness of the 0.5Mg-0.9Si alloy, but the improvement is not significant. By adjusting the Mg and Si content in the alloy, the 0.4Mg-0.7Si and 0.7Mg-0.7Si alloys exhibit a significant improvement in both strength and EC after aging treatment.

4 Conclusions

The influences of Mg and Si addition on the mechanical properties and EC of the Al-2.3Fe alloy were investigated through SEM, XRD, and thermodynamic calculations, covering as-cast, solid solution, and T6 heat-treated states. By analyzing the properties and microstructures of alloys with different Mg/Si ratios during the heat-treatment, the corresponding relationship between the Mg/Si ratio and the age-hardening effect was established, and a casting Al-2.3Fe alloy with both high EC and high strength was obtained.

(1) The addition of Mg will increase the solidification range of the Al-2.3Fe alloy, resulting in the formation of coarse lath-like $Al_{13}Fe_4$ phase. The combined addition of Mg and Si can effectively refine the second phase, and new α-AlFeSi phase and AlFeMgSi phase are formed, enhancing the second-phase strengthening effect of the alloy and improving its mechanical properties. However, the solid solution of elements will lead to a decrease in EC.

(2) Solution treatment causes the coarsening and spheroidization of the second phase, and age treatment further promotes this phenomenon. The continuity of the eutectic is disrupted, making the plastic deformation of the alloy non-uniform and leading to a rapid decrease in the elongation of the alloy.

(3) The age-hardening response of the Al-2.3Fe-*x*Mg-*y*Si alloys is jointly governed by the solid solubility of elements in the Al matrix and the content of second phases. When the Mg/Si ratio is 0.56, the alloy exhibits the optimal age strengthening effect. After T6 aging treatment, the 0.4Mg-0.7Si alloy (actual chemical composition Al-2.31Fe-0.40Mg-0.72Si) reaches a yield strength of 242.1±7.2 MPa and a tensile strength of 309.5±5.6 MPa at the peak aging state, and its EC increases to (52.4±0.6)% IACS.

Acknowledgments

This work was financially supported by the National Natural Science Foundation of China (U2102212 and 52422407), the Chongqing Science and Technology Commission of China (CSTC2024YCJH-BGZXM0041), and the Major Scientific and Technological Innovation Project of CITIC Group (2022ZXKYA06100).

Conflict of interest

The authors declare that they have no known competing financial interests or personal relationships that could have appeared to influence the work reported in this paper.

References

[1] Zhan H Y, Zeng G, Wang Q G, et al. Unified casting (UniCast) aluminum alloy – A sustainable and low-carbon materials solution for vehicle lightweighting. Journal of Materials Science & Technology, 2023, 154: 251–268.
[2] Ramesh P, and Lenin N C. High power density electrical machines for electric vehicles – comprehensive review based on material technology. IEEE Transactions on Magnetics, 2019, 55(11): 1–21.
[3] Li Y X, Hu A, Fu Y T, et al. Al alloys and casting processes for induction motor applications in battery-powered electric vehicles: A review. Metals, 2022, 12(2): 216.
[4] Khangholi S N, Javidani M, Maltais A, et al. Review on recent progress in Al-Mg-Si 6xxx conductor alloys. Journal of Materials Research, 2022, 37(3): 670–691.
[5] Luo Z G, Zhang X, Liu Z S, et al. Mechanical properties and interfacial characteristics of 6061 Al alloy plates fabricated by hot-roll bonding. International Journal of Minerals, Metallurgy and Materials, 2024, 31(8): 1890–1899.
[6] Luo Q, Li X, Li Q, et al. Achieving grain refinement of α-Al and Si modification simultaneously by La-B-Sr addition in Al-10Si alloys. Journal of Materials Science & Technology, 2023, 135: 97–110.
[7] Jeon J H, Bae D H. Effect of cooling rate on the thermal and electrical conductivities of an A356 sand cast alloy. Journal of Alloys and Compounds, 2019, 808: 151756.
[8] Bakhtiyarov S I, Overfelt R A, Teodorescu S G. Electrical and thermal conductivity of A319 and A356 aluminum alloys. Journal of Materials Science, 2001, 36: 4643–4648.
[9] Li Y, Jiang Y, Hu B, et al. Novel Al-Ti-Nb-B grain refiners with superior efficiency for Al-Si alloys. Scripta Materialia, 2020, 187: 262–267.
[10] Zhu L F, Zhang Y, Luo Q, et al. Effectively refining Al-10Si alloy via Al-Ti-Nb-B refiner with Nb_2O_5. Journal of Materials Science & Technology, 2024, 176: 204–210.
[11] Yang Y, Nie J F, Mao Q Z, et al. Improving the combination of electrical conductivity and tensile strength of Al 1070 by rotary swaging deformation. Results in Physics, 2019, 13: 102236.
[12] Pan L, Breton F, and Fourmann J. Development of a new Al-Fe-Ni alloy for electric vehicle applications. International Journal of Metalcasting, 2024, 18(4): 2841–2845.
[13] Wang Y, Zhu L J, Niu G D, et al. Conductive Al alloys: The contradiction between strength and electrical conductivity. Advanced Engineering Materials, 2021, 23(5): 2001249.
[14] Lunn K F, and Apelian D. Thermal and electrical conductivity of aluminum alloys: Fundamentals, structure-property relationships, and pathways to enhance conductivity. Materials Science and Engineering: A, 2025, 924: 147766.
[15] Dong Q P, Wang R Z, Wang J H, et al. Influence of Mg/Si ratio on the mechanical strength and electrical conductivity of Al-Mg-Si alloys. Materials Today Communications, 2025, 42: 111439.
[16] Cui X L, Ye H, Liu H Y, et al. The improvement mechanism of good matching between electrical conductivity and mechanical properties for Al-4Si-0.8Mg-0.6Fe alloy. Journal of Alloys and Compounds, 2023, 938: 168275.
[17] Wang H, Li Y D, Zhang M, et al. Preheating-assisted solid-state friction stir repair of Al-Mg-Si alloy plate at different rotational speeds. International Journal of Minerals, Metallurgy and Materials, 2024, 31(4): 725–736.
[18] Dong Q P, Zhang Y, Wang J H, et al. Enhanced strength-conductivity trade-off in Al-Mg-Si alloys with optimized Mg/Si ratio. Journal of Alloys and Compounds, 2024, 970: 172682.

[19] Singh P, Ramacharyulu D A, Kumar N, et al. Change in the structure and mechanical properties of Al-Mg-Si alloys caused by the addition of other elements: A comprehensive review. Journal of Materials Research and Technology, 2023, 27: 1764–1796.
[20] Li X L, Scherf A, Heilmaier M, et al. The Al-rich part of the Fe-Al phase diagram. Journal of Phase Equilibria and Diffusion, 2016, 37(2): 162–173.
[21] Jiang H X, Li S X, Zheng Q J, et al. Effect of minor lanthanum on the microstructures, tensile and electrical properties of Al-Fe alloys. Materials & Design, 2020, 195: 108991.
[22] Liu S F, Hu A, Hu H. Potential Al-Fe cast alloys for motor applications in electric vehicles: An overview. Key Engineering Materials, 2022, 923: 3–19.
[23] Hou J P, Li R, Wang Q, et al. Origin of abnormal strength-electrical conductivity relation for an Al-Fe alloy wire. Materialia, 2019, 7: 100403.
[24] Jiang X Y, Zhang Y, Yi D Q, et al. Low-temperature creep behavior and microstructural evolution of 8030 aluminum cables. Materials Characterization, 2017, 130: 181–187.
[25] Kim D H, Kim J H, and Kobayashi E. Enhanced mechanical properties of Al-Si-Cu-Mg(-Fe) alloys by a deformation-semisolid extrusion process. Materials Science and Engineering: A, 2021, 825: 141667.
[26] Chen P, Fan X Z, Yang Q B, et al. Creep behavior and microstructural evolution of 8030 aluminum alloys compressed at intermediate temperature. Journal of Materials Research and Technology, 2021, 12: 1755–1761.
[27] Luo G, Zhou X, Li C B, et al. Design and preparation of Al-Fe-Ce ternary aluminum alloys with high thermal conductivity. Transactions of Nonferrous Metals Society of China, 2022, 32(6): 1781–1794.
[28] Kong Y P, Jia Z H, Liu Z P, et al. Effect of Zr and Er on the microstructure, mechanical and electrical properties of Al-0.4Fe alloy. Journal of Alloys and Compounds, 2021, 857: 157611.
[29] Shi Z M, Gao K, Shi Y T, et al. Microstructure and mechanical properties of rare-earth-modified Al-1Fe binary alloys. Materials Science and Engineering: A, 2015, 632: 62–71.
[30] Shin J S, Ko S H, Kim K T. Development and characterization of low-silicon cast aluminum alloys for thermal dissipation. Journal of Alloys and Compounds, 2015, 644: 673–686.
[31] Qin L M, Tang P, Meng S X. Effect of Ni addition on the microstructure, conductivities and mechanical properties of as-cast Al-Fe alloys. Journal of Alloys and Compounds, 2024, 986: 174160.
[32] Zhang Y F, Luo X L, Zhu L F, et al. Design of non-heat-treatable Al-Fe-Ni alloys with high electrical conductivity and high strength via CALPHAD approach. Journal of Alloys and Compounds, 2024, 1009: 176920.
[33] Bian Z Y, Dai S H, Wu L, et al. Thermal stability of Al-Fe-Ni alloy at high temperatures. Journal of Materials Research and Technology, 2019, 8(3): 2538–2548.
[34] Bian Z Y, Liu Y T, Dai S H, et al. Regulating microstructures and mechanical properties of Al-Fe-Ni alloys. Progress in Natural Science: Materials International, 2020, 30(1): 54–62.
[35] Trink B, Weißensteiner I, Uggowitzer P J, et al. Processing and microstructure-property relations of Al-Mg-Si-Fe crossover alloys. Acta Materialia, 2023, 257: 119160.
[36] Tao G H, Liu C H, Chen J H, et al. The influence of Mg/Si ratio on the negative natural aging effect in Al-Mg-Si-Cu alloys. Materials Science and Engineering: A, 2015, 642: 241–248.
[37] Jiang H X, Li S X, Zhang L L, et al. The influence of rare earth element lanthanum on the microstructures and properties of as-cast 8176 (Al-0.5Fe) aluminum alloy. Journal of Alloys and Compounds, 2021, 859: 157804.
[38] Algendy A Y, Javidani M, Khangholi S N, et al. Enhanced mechanical strength and electrical conductivity of Al-Ni-based conductor cast alloys containing Mg and Si. Advanced Engineering Materials, 2024, 26(1): 2301241.
[39] Cui X L, Li X H, Ye H, et al. Study on microstructure characterization, electrical conductivity and mechanical property improvement mechanisms of a novel Al-Si-Mg-Fe-Cu alloy. Journal of Alloys and Compounds, 2021, 885: 160959.
[40] Tang L P, Wei P F, Hu Z L, et al. Microstructure and mechanical properties stability of pre-hardening treatment in Al-Cu alloys for pre-hardening forming process. International Journal of Minerals, Metallurgy and Materials, 2024, 31(3): 539–551.
[41] Xu X X, Yang Z, Ye Y L, et al. Effects of various Mg/Si ratios on microstructure and performance property of Al-Mg-Si alloy cables. Materials Characterization, 2016, 119: 114–119.
[42] Zhang B, Wu L L, Wan B, et al. Structural evolution, mechanical properties, and electronic structure of Al-Mg-Si compounds from first principles. Journal of Materials Science, 2015, 50(19): 6498–6509.
[43] Marioara C D, Andersen S J, Hell C, et al. Atomic structure of clusters and GP-zones in an Al-Mg-Si alloy. Acta Materialia, 2024, 269: 119811.